J. Fluid Mech. (2017), *vol.* 830, *pp.* 387–407.
doi:10.1017/jfm.2017.601

Green's functions for Rossby waves

R. C. Kloosterziel[1,†] **and L. R. M. Maas**[2,3]

[1]School of Ocean and Earth Science and Technology, University of Hawaii, Honolulu, HI 96822, USA

[2]Institute for Marine and Atmospheric Research, Utrecht University, Princetonplein 5, 3584CC Utrecht, The Netherlands

[3]Royal Netherlands Institute for Sea Research, P.O. Box 59, 1790AB Texel, The Netherlands

(Received 18 April 2017; revised 18 July 2017; accepted 21 August 2017;
first published online 2 October 2017)

Compact solutions are presented for planetary, non-divergent, barotropic Rossby waves generated by (i) an impulsive point source and (ii) a sustained point source of curl of wind stress. Previously, only cumbersome integral expressions were known, rendering them practically useless. Our simple expressions allow for immediate numerical visualization/animation and further mathematical analysis.

Key words: geophysical and geological flows, rotating flows, waves in rotating fluids

1. Introduction

Non-divergent waves in a two-dimensional fluid layer on a rotating sphere, restored solely by Coriolis forces due to vorticity conservation, are present as second-class waves in Laplace's equations and were studied by Margules (1893) and Hough (1898). Their nature was clarified when Rossby & Collaborators (1939) derived a simplified version of the barotropic vorticity equation on a mid-latitude tangent plane (β-plane). They eliminated the first-class gravity waves by assuming a rigid lid. Thus they considered non-divergent flow in a fluid layer in which vorticity changes in time due to advection of variations in background planetary vorticity. Linear, free-wave solutions of this equation display strictly westward phase propagation, but west or eastward energy propagation for long and short waves, respectively. In recognition of the value of this clarification, these waves are today called Rossby waves. They are forced by the curl of the wind stress and the barotropic non-divergent linear motions are governed by

$$\partial_t q + \beta v = \mathrm{curl}\,\boldsymbol{\tau}. \tag{1.1}$$

The relative vorticity $q = \partial_x v - \partial_y u$ is created by south–north advection of planetary vorticity and by $\boldsymbol{\tau} = \{\tau_x, \tau_y\}$ the wind-stress vector (see e.g. Veronis 1958; Pedlosky 1987). As usual, t is time, x longitude, y latitude and βv is the advection of planetary vorticity by the latitudinal (south–north) velocity component v.

Introducing a streamfunction ψ, so that the velocity components are $u = -\partial_y\psi$, $v = \partial_x\psi$ and $q = \nabla^2\psi$, equation (1.1) becomes $\partial_t\nabla^2\psi + \beta\partial_x\psi = \mathrm{curl}\,\boldsymbol{\tau}$ with $\nabla^2 = (\partial_x^2 + \partial_y^2)$.

† Email address for correspondence: rudolf@soest.hawaii.edu

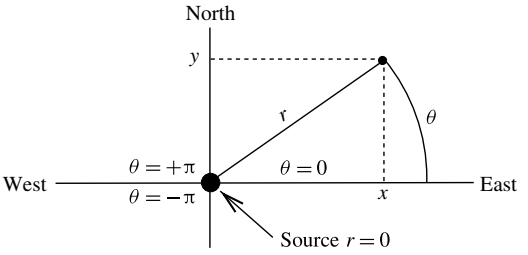

FIGURE 1. The Cartesian $\{x, y\}$ and cylindrical $\{r, \theta\}$ coordinate systems. The forcing location for G_δ and G_H at $r = 0$ is indicated by ●. 'East' is defined by $\theta = 0$, 'west' by $\theta = \pm\pi$, 'north' by $\theta = \pi/2$, r is the distance from the source and $x = r\cos\theta$, $y = r\sin\theta$.

In this study, the Green's function G_δ for an 'impulsive point source' and G_H for a 'switch-on point source' are defined as solutions of

$$\mathcal{L}G_\delta = \delta(t)\delta(x)\delta(y), \quad \mathcal{L}G_H = H(t)\delta(x)\delta(y), \quad \mathcal{L} = \partial_t\nabla^2 + \beta\partial_x. \tag{1.2a–c}$$

$\mathcal{L}$ is the Rossby wave operator, δ the usual Dirac delta function and H the Heaviside unit step function and by definition $\delta(t) \equiv \mathrm{d}H(t)/\mathrm{d}t$. In this paper we shall show that

$$G_\delta = \frac{H(t)}{4}[\mathrm{J}_0(z_+)\mathrm{Y}_0(z_-) + \mathrm{J}_0(z_-)\mathrm{Y}_0(z_+)], \tag{1.3}$$

$$G_H = \frac{tH(t)}{2(z_+^2 - z_-^2)}\,[z_+\mathrm{J}_1(z_+)\mathrm{Y}_0(z_-) - z_-\mathrm{J}_1(z_-)\mathrm{Y}_0(z_+) + z_+\mathrm{J}_0(z_-)\mathrm{Y}_1(z_+) - z_-\mathrm{J}_0(z_+)\mathrm{Y}_1(z_-)]\,. \tag{1.4}$$

In (1.3) and (1.4) J_n, Y_n are nth-order Bessel functions of the first and second kind, respectively, with complex conjugate arguments

$$z_+ = \sqrt{\beta t r}\mathrm{e}^{+\mathrm{i}\theta/2}, \quad z_- = \sqrt{\beta t r}\mathrm{e}^{-\mathrm{i}\theta/2} \quad \text{or} \quad z_\pm = \sqrt{\beta t(x \pm \mathrm{i}y)}. \tag{1.5a–c}$$

The usual cylindrical coordinate system $\{r, \theta\}$ is employed with the origin at the forcing location (see figure 1). The prefactor $H(t)$ in (1.3) and (1.4) enforces 'causality', i.e. $G_{\delta,H} = 0$ for $t < 0$. Since efficient algorithms for Bessel functions exist, the compact expressions in (1.3) and (1.4) allow for a quick evaluation: with a few lines of code in little time a movie can be created visualizing the temporal and spatial evolutions.

Typically in finding Green's functions and solutions of linear partial differential equations like (1.2), the well-established theory for Laplace and/or Fourier transforms is used in combination with the theory of differential equations. Various integral representations for G_δ and G_H that have been derived in such a manner are briefly reviewed in § 2. They also reveal a relation between G_δ and G_H: not only is $\partial_t G_H = G_\delta$, as expected, but once G_δ is known G_H follows by differentiation of G_δ with respect to the polar angle θ. Precise numerical evaluation of the integral representation is cumbersome, but for locations exactly east ($\theta = 0$) and west ($\theta = \pm\pi$) of the source they can be evaluated exactly. Our new expressions for G_δ and G_H provide a complete 'picture' at any angle θ with the east–west axis.

The compact formula (1.3) for G_δ was discovered by recognizing that a particular integral representation of G_δ is essentially an integral of the kind studied by

Dixon & Ferrar (1933). Differentiation of (1.3) then quickly yielded G_H given by (1.4). This is discussed in § 3 where, for completeness' sake, we also show that the Green's functions given by (1.3) and (1.4) indeed solve (1.2). In § 4 we provide illustrative graphs of G_δ and G_H and derive simple approximations which presume large arguments $|z_\pm|$ or $\sqrt{\beta tr} \gg 1$. Also in § 4 the associated wave–energy density distributions are considered. In § 5 we discuss the ramifications of this study and in particular we draw attention to results that indicate that parabolic coordinates $\zeta = \sqrt{r+x}$, $\eta = \sqrt{r-x}$ appear to be a natural choice when studying non-divergent Rossby waves.

2. Integral representations and relations between G_δ and G_H

Veronis (1958) showed that

$$G_\delta = -\frac{H(t)}{\pi} \int_0^\infty \frac{\mathrm{J}_0\left(2\sqrt{\beta tr\left(\eta^2 + \cos^2\tfrac{1}{2}\theta\right)}\right)}{\sqrt{\eta^2+1}}\,\mathrm{d}\eta, \tag{2.1}$$

correcting for a typographical error. He called the point-size burst of wind-stress curl a 'tweak' and derived (2.1) through the use of a Laplace transform in time of (1.2*a*) which reduced the problem to solving a second-order partial differential equation (in variables x, y). With the solution at hand, equation (2.1) followed from the inverse Laplace transform. Longuet-Higgins (1965) also found (2.1), but through a triple Fourier transform. Much later, Kamenkovich (1989) established that

$$G_H = -\frac{H(t)}{\pi}\sqrt{\frac{t}{\beta r}} \int_0^\infty \frac{\mathrm{J}_1\left(2\sqrt{\beta tr\left(\eta^2 + \cos^2\tfrac{1}{2}\theta\right)}\right)}{\sqrt{\eta^2+1}\sqrt{\eta^2+\cos^2\tfrac{1}{2}\theta}}\,\mathrm{d}\eta, \tag{2.2}$$

using a Laplace transform of (1.2*b*) with respect to time. Both infinite integrals defining $G_{\delta,H}$ are difficult to evaluate numerically due to the oscillatory behaviour of J_0, J_1 for increasing η. However, computationally more efficient integral expressions for G_δ have been found by Llewellyn-Smith (1997).

The integral representation (2.1) for G_δ reduces on the east–west axis to

$$\theta = 0 \text{ (east)}: \quad G_\delta = \frac{\mathrm{J}_0(\sqrt{\beta tr})\mathrm{Y}_0(\sqrt{\beta tr})}{2}, \tag{2.3a}$$

$$\theta = \pm\pi \text{ (west)}: \quad G_\delta = -\frac{\mathrm{I}_0(\sqrt{\beta tr})\mathrm{K}_0(\sqrt{\beta tr})}{\pi}, \tag{2.3b}$$

with I_n, K_n the nth-order modified Bessel functions of the first and second kind, respectively. For convenience we have dropped the 'causality switch' $H(t)$. The limiting case $\theta = \pm\pi$ (2.3*b*) was first noted, apart from a missing minus sign, by Longuet-Higgins (1965) but for $\theta = 0$ he erred. The correct limit $\theta = 0$ in (2.3*a*) was given by Llewellyn-Smith (1997). Kamenkovich (1989) recognized with the integral representation (2.2) that G_H reduces on the east–west axis to

$$\theta = 0 \text{ (east)}: \quad G_H = \frac{t}{2}[\mathrm{J}_0(\sqrt{\beta tr})\mathrm{Y}_0(\sqrt{\beta tr}) + \mathrm{J}_1(\sqrt{\beta tr})\mathrm{Y}_1(\sqrt{\beta tr})], \tag{2.4a}$$

$$\theta = \pm\pi \text{ (west)}: \quad G_H = -\frac{t}{\pi}[\mathrm{I}_0(\sqrt{\beta tr})\mathrm{K}_0(\sqrt{\beta tr}) + \mathrm{I}_1(\sqrt{\beta tr})\mathrm{K}_1(\sqrt{\beta tr})]. \tag{2.4b}$$

Simpler integral expressions

$$G_\delta = -\frac{1}{4\pi}\int_{-\infty}^{+\infty} \mathrm{J}_0(\sqrt{2\beta tr(\cosh\nu+\cos\theta)})\,\mathrm{d}\nu, \tag{2.5a}$$

$$G_H = -\frac{t}{2\pi}\int_{-\infty}^{+\infty} \frac{\mathrm{J}_1(\sqrt{2\beta tr(\cosh\nu+\cos\theta)})}{\sqrt{2\beta tr(\cosh\nu+\cos\theta)}}\mathrm{d}\nu, \tag{2.5b}$$

follow from (2.1) and (2.2) through substitution of $\eta = \sinh 1/2\nu$. Note that G_δ is a function of the similarity variables βtx, βty or $G_\delta = F(\beta tr, \theta)$ while G_H is of the form $tF(\beta tr, \theta)$.

To proceed, observe how on the east side ($\theta = 0$), the integral expression (2.5a) for G_δ simplifies to

$$\begin{aligned} G_\delta &= -\frac{1}{4\pi}\int_{-\infty}^{+\infty} \mathrm{J}_0\left(2\sqrt{\beta tr}\,\cosh\frac{1}{2}\nu\right)\,\mathrm{d}\nu \\ &= -\frac{1}{2\pi^2}\iint_{-\infty}^{+\infty} \sin(2\sqrt{\beta tr}\,\cosh\nu'\cosh\mu)\,\mathrm{d}\nu'\,\mathrm{d}\mu, \end{aligned} \tag{2.6}$$

where we use $\nu' = (1/2)\nu$, and the first of the integral expressions for the Bessel functions

$$\mathrm{J}_0(x) = \frac{1}{\pi}\int_{-\infty}^{+\infty}\sin(x\,\cosh\mu)\,\mathrm{d}\mu, \quad \mathrm{Y}_0(x) = -\frac{1}{\pi}\int_{-\infty}^{+\infty}\cos(x\,\cosh\mu)\,\mathrm{d}\mu. \tag{2.7a,b}$$

Setting $m = \mu + \nu'$, $n = \mu - \nu'$, we rotate integration variables μ, ν' over $\pi/4$, yielding

$$G_\delta = -\frac{1}{4\pi^2}\int_{-\infty}^{+\infty}\int_{-\infty}^{+\infty}\sin(\sqrt{\beta tr}[\cosh m+\cosh n])\,\mathrm{d}m\,\mathrm{d}n. \tag{2.8}$$

Using the trigonometric identity $\sin(a+b) = \sin a\cos b + \sin b\cos a$, this integral is separable and leads, with the Bessel identities (2.7a,b), to (2.3a), i.e.

$$\begin{aligned} G_\delta &= -\frac{1}{4\pi^2}\left(\int_{-\infty}^{+\infty}\sin(\sqrt{\beta tr}\cosh m)\,\mathrm{d}m\int_{-\infty}^{+\infty}\cos(\sqrt{\beta tr}\cosh n)\mathrm{d}n\right. \\ &\quad \left. + \int_{-\infty}^{+\infty}\cos(\sqrt{\beta tr}\cosh m)\,\mathrm{d}m\int_{-\infty}^{+\infty}\sin(\sqrt{\beta tr}\cosh n)\,\mathrm{d}n\right) = \frac{\mathrm{J}_0(\rho)\mathrm{Y}_0(\rho)}{2}, \end{aligned} \tag{2.9}$$

with $\rho \equiv \sqrt{\beta tr}$. A similar derivation can be used to obtain the established result (2.3b) on the west axis ($\theta = \pm\pi$).

Since G_H describes the response to sustained forcing represented by the Heaviside function $H(t)$ and G_δ to impulsive forcing represented by $\delta(t)$, one expects $G_\delta = \partial G_H/\partial t$. The integral representations for G_δ and G_H confirm this. For example, in (2.5b)

$$G_H = \frac{1}{2\pi}\int_{-\infty}^{+\infty}\frac{t\mathrm{J}_0'(z)}{z}\,\mathrm{d}\nu, \quad z \equiv \sqrt{2\beta tr(\cosh\nu+\cos\theta)}, \tag{2.10}$$

where we used the fact that $\mathrm{J}_1 = -\mathrm{J}_0'$ (a prime indicates differentiation). Since $\partial z/\partial t = z/2t$, it follows that

$$\frac{\partial G_H}{\partial t} = \frac{1}{2\pi}\left[\int \frac{\mathrm{J}_0'(z)}{z}\mathrm{d}\nu + \int t\left(\frac{\mathrm{J}_0''(z)}{z}\frac{z}{2t} - \frac{\mathrm{J}_0'(z)}{z^2}\frac{z}{2t}\right)\mathrm{d}\nu\right]$$
$$= \frac{1}{2\pi}\left[\int \frac{1}{2}\left(\frac{\mathrm{J}_0'(z)}{z} + \mathrm{J}_0''(z)\right)\mathrm{d}\nu\right] = -\frac{1}{4\pi}\int \mathrm{J}_0(z)\,\mathrm{d}\nu = (2.5a) = G_\delta \qquad (2.11)$$

because J_0 solves the Bessel equation $z^2\mathrm{J}_0'' + z\mathrm{J}_0' + z^2\mathrm{J}_0 = 0$.

Another relation exists between G_δ and G_H: in (2.5*b*)

$$\frac{t\mathrm{J}_1(z)}{z} = \frac{1}{\beta r\sin\theta}\frac{\partial \mathrm{J}_0(z)}{\partial\theta}. \qquad (2.12)$$

Comparison with (2.5*a*) shows that

$$G_H = \frac{2}{\beta r\sin\theta}\frac{\partial G_\delta}{\partial\theta} \quad \text{and} \quad \left(\frac{\partial^2}{\partial t\partial\theta} - \frac{1}{2}\beta r\sin\theta\right)G_H = 0 \qquad (2.13a,b)$$

because $G_\delta = \partial_t G_H$. Time differentiation shows that therefore G_δ also satisfies (2.13*b*).

3. Closed-form expressions for G_δ and G_H

In view of the definition of $z_\pm$ in (1.5), the integral representation (2.5*a*) equals

$$G_\delta = -\frac{1}{4\pi}\int_{-\infty}^{+\infty} \mathrm{J}_0\left(\sqrt{z_+^2 + z_-^2 + 2z_+z_-\cosh\nu}\right)\mathrm{d}\nu. \qquad (3.1)$$

This observation led us to the expression (1.3) for G_δ as follows. Dixon & Ferrar (1933) considered products of modified Bessel functions of the second kind $\mathrm{K}_{\nu,\mu}$ and showed that such products can be reduced to a single integral involving $\mathrm{K}_{\nu+\mu}$, provided certain conditions are met. For the purpose of this paper it suffices to point out that one of their results implies that for real $x, y > 0$

$$\mathrm{K}_0(\mathrm{i}x)\mathrm{K}_0(\mathrm{i}y) = \int_{-\infty}^{+\infty} \mathrm{K}_0(\mathrm{i}\lambda)\,\mathrm{d}t', \quad \lambda = \sqrt{x^2 + y^2 + 2xy\cosh 2t'} \qquad (3.2)$$

(Dixon & Ferrar 1933, formula 3.32). Connection formulas tell us further that

$$\mathrm{K}_0(z) = -\tfrac{1}{2}\pi\mathrm{i}H_0^{(2)}(-\mathrm{i}z), \quad -\tfrac{1}{2}\pi \leqslant \mathrm{ph}\,z \leqslant \pi, \qquad (3.3)$$

with the Hankel function $H_0^{(2)} = \mathrm{J}_0 - \mathrm{i}\mathrm{Y}_0$ (see the *NIST Handbook of Mathematical Functions*, Olver *et al.* (2010), formula 10.27.8). Specifically this means $\mathrm{K}_0(\mathrm{i}x) = -(1/2)\pi\mathrm{i}H_0^{(2)}(x)$ and likewise for y. Therefore with (3.2) it follows that

$$\int_{-\infty}^{+\infty}[\mathrm{J}_0(\lambda) - \mathrm{i}\mathrm{Y}_0(\lambda)]\,\mathrm{d}t' = \int_{-\infty}^{+\infty} H_0^{(2)}(\lambda)\,\mathrm{d}t' = -\frac{\pi\mathrm{i}}{2}H_0^{(2)}(x)H_0^{(2)}(y)$$
$$= -\frac{\pi}{2}[\mathrm{J}_0(x)\mathrm{Y}_0(y) + \mathrm{J}_0(y)\mathrm{Y}_0(x)] - \frac{\pi\mathrm{i}}{2}[\mathrm{J}_0(x)\mathrm{J}_0(y) - \mathrm{Y}_0(x)\mathrm{Y}_0(y)] \qquad (3.4)$$

(for the more general case involving $H_\nu^{(2)}(x)H_\mu^{(2)}(y)$ see formula 17.4.2 (76) in Erdélyi (1953) and for related results Magnus, Oberhettinger & Soni (1966), p. 93, which however contains a typographical error). Equating real parts in (3.4) leads to the

product $\mathrm{J}_0(x)\mathrm{Y}_0(y)+\mathrm{J}_0(y)\mathrm{Y}_0(x)$ expressed as an integral over $\mathrm{J}_0(\lambda)$. Comparison with the integral expression (3.1) shows that the closed-form expression (1.3) would follow if we could simply substitute $x=z_+$, $y=z_-$ in (3.4) after setting $\nu=2t'$ in (3.1). Thus we surmised that G_δ given in (1.3) is the solution of (1.2*a*). This 'educated guess' proved to be correct by direct verification (see below).

However, Llewellyn Smith (University of California, San Diego) pointed out during the revision process of this manuscript that the results of Dixon & Ferrar (1933) in fact imply that (3.1) equals (1.3) when the principle of analytic continuation is invoked. Again tailored specifically to our needs here, Dixon & Ferrar (1933) state that for complex variables Z, z with positive real parts (absolute phase $<\pi/2$)

$$\mathrm{K}_0(Z)\mathrm{K}_0(z)=\int_{-\infty}^{+\infty}\mathrm{K}_0\left(\sqrt{Z^2+z^2+2Zz\,\cosh 2t'}\right)\mathrm{d}t',\quad |\mathrm{ph}\,Z,\,z|<\frac{\pi}{2}. \tag{3.5a,b}$$

The Bessel functions are analytic when a branch cut is made on the negative real axis, i.e. for $\mathbb{C}\backslash(-\infty,0]$. If we exclude the west axis ($\theta=\pm\pi$), equation (3.5) is valid when $Z=z_+$, $z=z_-$ is substituted (for $\theta=\pi$ we have $z_\pm=\pm\mathrm{i}\sqrt{\beta tr}$ and for $\theta=-\pi$ we have $z_\pm=\mp\mathrm{i}\sqrt{\beta tr}$ according to (1.5)). Both variables lie in the open right half of the complex plane and if rotated anti-clockwise by an angle ϕ they become $z'_\pm=\mathrm{e}^{\mathrm{i}\phi}z_\pm$. For $\phi=\pi/2$ the rotated $z'_\pm=\mathrm{i}z_\pm$ have been moved to the upper half of the complex plane without crossing the negative real axis. Therefore the left-hand side of (3.5) remains analytic. The argument of K_0 in the integral becomes under this rotation simply $\mathrm{e}^{\mathrm{i}\phi}\sqrt{2\beta tr(\cos\theta+\cosh 2t')}$. Thus, if the west axis is excluded from consideration, as ϕ is increased towards $\pi/2$ the argument never crosses the branch cut of K_0 and the integrand and the integral on the right-hand side of (3.5) remain analytic. By analytic continuation we therefore find that

$$\mathrm{K}_0(\mathrm{i}z_+)\mathrm{K}_0(\mathrm{i}z_-)=\int_{-\infty}^{+\infty}\mathrm{K}_0\left(\mathrm{i}\sqrt{z_+^2+z_-^2+2z_+z_-\,\cosh 2t'}\right)\mathrm{d}t'. \tag{3.6}$$

The conditions for (3.3) to be valid are met and we can, just as shown above for real x, y, equate the real parts on the left and right in (3.6). This establishes that the integral representation (3.1) equals the closed-form expression (1.3) for G_δ. Despite this compelling argument, we nonetheless verify the validity of (1.3) below and show how G_H (1.4) was derived.

3.1. *Validation of* G_δ

In order to verify that G_δ (1.3) is correct, it is expedient to write the complex conjugate variables $z_\pm$ introduced in (1.5) as

$$z_+=az_\star,\quad z_-=a\bar{z}_\star,\quad a=\sqrt{\frac{\beta t}{2}},\quad z_\star\equiv\zeta+\mathrm{i}\eta,\quad \bar{z}_\star\equiv\zeta-\mathrm{i}\eta, \tag{3.7a–e}$$

with parabolic coordinates

$$\zeta=\sqrt{r(1+\cos\theta)}=\sqrt{r+x},\quad \eta=\sqrt{r(1-\cos\theta)}=\sqrt{r-x}. \tag{3.8a,b}$$

Lines of constant ζ are parabolas that open towards the west ($x<0$) and constant η parabolas that open towards the east ($x>0$) as sketched in figure 2. The Laplace

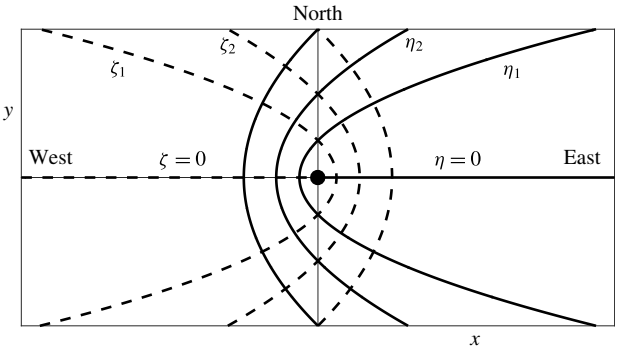

FIGURE 2. The parabolic coordinate system $\{\zeta, \eta\}$ with $\zeta = \sqrt{r+x}$, $\eta = \sqrt{r-x}$ defined in (3.8). The entire western axis $x < 0$, $y = 0$ coincides with $\zeta = 0$, the eastern axis $x > 0$, $y = 0$ with $\eta = 0$. The origin $\zeta = \eta = 0$ indicated by ● is the forcing location as in figure 1.

operator in these coordinates is well known (see Moon & Spencer 1961) while $\partial/\partial x$ is easily calculated with the chain rule. They are

$$\nabla^2 = \frac{1}{\zeta^2+\eta^2}\left[\frac{\partial^2}{\partial\zeta^2}+\frac{\partial^2}{\partial\eta^2}\right], \quad \frac{\partial}{\partial x} = \frac{1}{2r}\left[\zeta\frac{\partial}{\partial\zeta}-\eta\frac{\partial}{\partial\eta}\right]. \tag{3.9a,b}$$

But $2r = \zeta^2+\eta^2$ and the Rossby wave operator becomes

$$\mathcal{L} = \frac{1}{\zeta^2+\eta^2}\left\{\frac{\partial}{\partial t}\left(\frac{\partial^2}{\partial\zeta^2}+\frac{\partial^2}{\partial\eta^2}\right)+\beta\left(\zeta\frac{\partial}{\partial\zeta}-\eta\frac{\partial}{\partial\eta}\right)\right\}. \tag{3.10}$$

With a few elementary manipulations one finds next that

$$\mathcal{L} = \frac{1}{z_\star\bar{z}_\star}\left\{4\frac{\partial}{\partial t}\left(\frac{\partial^2}{\partial z_\star\partial\bar{z}_\star}\right)+\beta\left(\bar{z}_\star\frac{\partial}{\partial z_\star}+z_\star\frac{\partial}{\partial\bar{z}_\star}\right)\right\}. \tag{3.11}$$

With (3.11) it follows, after collecting terms, that

$$\begin{aligned}\mathcal{L}\,\mathrm{J}_0(z_+)\mathrm{Y}_0(z_-) \;=\; &\frac{\beta}{z_\star\bar{z}_\star}\left\{\mathrm{J}_0'(z_+)[z_-\mathrm{Y}_0''(z_-)+\mathrm{Y}_0'(z_-)+z_-\mathrm{Y}_0(z_-)]\right.\\ &\left.+\,\mathrm{Y}_0'(z_-)[z_+\mathrm{J}_0''(z_+)+\mathrm{J}_0'(z_+)+z_+\mathrm{J}_0(z_+)]\right\}=0\end{aligned} \tag{3.12}$$

because J_0, Y_0 satisfy the Bessel equation

$$z^2\mathcal{J}_0''+z\mathcal{J}_0'+z^2\mathcal{J}_0=0. \tag{3.13}$$

Clearly also $\mathcal{L}\mathrm{J}_0(z_-)\mathrm{Y}_0(z_+)=0$ and away from $z_\star\bar{z}_\star = 2r = 0$ for $t > 0$ indeed $\mathcal{L}G_\delta = 0$.

The $\delta(t)\delta(x)\delta(y)$ singularity in (1.2*a*) has to come from the term $\partial_t\nabla^2 G_\delta$. The $\delta(t)$ behaviour must be associated with the time derivative of $H(t)$ which multiplies $\mathrm{J}_0(z_+)\mathrm{Y}_0(z_-)+\mathrm{J}_0(z_-)\mathrm{Y}_0(z_+)$ in (1.3). Replacing $\delta(x)\delta(y)$ on the right-hand side of (1.2*a*) by $\delta(r)/(2\pi r)$, for small r the Green's function must therefore behave as $G_\delta \approx H(t)\ln r/2\pi$. That this is true is seen as follows: since for small z

$$z\to 0: \quad \mathrm{J}_0(z)\approx 1, \quad \mathrm{Y}_0(z)\approx(2/\pi)\ln z, \tag{3.14a,b}$$

near the origin

$$r\downarrow 0:\quad G_\delta \approx \frac{H(t)}{4}\left[\frac{2}{\pi}\ln z_- + \frac{2}{\pi}\ln z_+\right] = \frac{H(t)}{2\pi}\ln \beta t r = \frac{H(t)}{2\pi}[\ln r + \ln \beta t] \tag{3.15}$$

because, according to (1.5), $z_\pm = \sqrt{\beta t r e^{\pm i\theta}}$. The part that only depends on time t plays no role in getting $\delta(t)\delta(x)\delta(y)$ from $\partial_t \nabla^2 G$ and therefore (1.3) has the correct behaviour near the origin. Finally, on the x axis in the limit $\theta \to 0$ (east) we have $z_+ = z_- = \sqrt{\beta t r}$ and it is seen with (1.3) that for $t > 0$ (2.3*a*) is recovered. For $\theta \to \pi$ (west) we have $z_\pm = \pm i\sqrt{\beta t r}$ and connection formulas are needed. They imply that $J_0(z_\pm) \to I_0(\sqrt{\beta t r})$ and that

$$\theta \to \pi:\quad Y_0(z_+) \to iI_0(\sqrt{\beta t r}) - \frac{2}{\pi}K_0(\sqrt{\beta t r}),\quad Y_0(z_-) \to -iI_0(\cdots) - \frac{2}{\pi}K_0(\cdots) \tag{3.16a,b}$$

(see the *NIST Handbook of Mathematical Functions* (Olver *et al.* 2010), formulas 10.27.6 and 10.27.11). Substituting this in (1.3) we find (2.3*b*). The same result is found in the limit $\theta = -\pi$. This proves that G_δ is correct.

3.2. *Derivation and validation of* G_H

The integral representations showed that G_H can be obtained through differentiation of G_δ according to (2.13*a*). With the $\{z_\star, \bar{z}_\star\}$ variables we find that (2.13*a*) becomes

$$G_H = -\frac{4}{\beta(z_\star^2 - \bar{z}_\star^2)}\left[z_\star \frac{\partial}{\partial z_\star} - \bar{z}_\star \frac{\partial}{\partial \bar{z}_\star}\right] G_\delta. \tag{3.17}$$

Substitution of $G_\delta = (1/4)\,[J_0(az_\star)Y_0(a\bar{z}_\star) + \text{c.c.}]$ results in the expression (1.4) for G_H with the definition of $z_\pm$ given in (3.7) and use of the fact that $J_0' = -J_1$ and $Y_0' = -Y_1$. Also the integral representations implied $\partial_t G_H = G_\delta$. According to (3.17) this is true if

$$G_\delta = -\frac{2t}{z_+^2 - z_-^2}\left[z_+ \frac{\partial}{\partial z_+} - z_- \frac{\partial}{\partial z_-}\right]\frac{\partial G_\delta}{\partial t}, \tag{3.18}$$

having restored $z_\pm$ on the right-hand side. We find, for example, that

$$\left.\begin{aligned} &\frac{\partial J_0(z_+)Y_0(z_-)}{\partial t} = \left[z_+ J_0'(z_+)Y_0(z_-) + z_- J_0(z_+)Y_0'(z_-)\right]/2t \quad \text{and} \\ &\left[z_+ \frac{\partial}{\partial z_+} - z_- \frac{\partial}{\partial z_-}\right]\frac{\partial J_0(z_+)Y_0(z_-)}{\partial t} = -\frac{z_+^2 - z_-^2}{2t}J_0(z_+)Y_0(z_-) \end{aligned}\right\} \tag{3.19}$$

after use of the Bessel equation (3.13). It quickly follows with (1.3) for G_δ that indeed $\partial_t G_H = G_\delta$. Moreover, since we know $\mathcal{L}G_\delta = 0$ for $r \neq 0$ and therefore $\partial_t \mathcal{L}G_H = 0$, it follows that $\mathcal{L}G_H = 0$ ($\mathcal{L}G_H = f(x, y) \neq 0$ can be ruled out).

The singularity at the origin has to come from $\partial_t \nabla^2 G_H$ in (1.2*b*) and the factor $H(t)$ on the right-hand side must be due to a time derivative of $tH(t)$. Therefore for small r the Green's function must behave as $G_H \approx tH(t)\ln r/2\pi$. That this is true follows with (3.14) for J_0, Y_0 and the fact that

$$z \to 0:\quad J_1(z) \sim z/2,\quad Y_1(z) \sim -2/(\pi z) + (z/\pi)\ln z. \tag{3.20a,b}$$

When put in (1.4), we find that for small r

$$r \downarrow 0: \quad G_H \approx \frac{tH(t)}{2\pi}[\ln r + \ln \beta t]. \tag{3.21}$$

Again the part that only depends on t is irrelevant, and G_H has the correct singularity.

Finally, it is easily verified with the Bessel equation (3.13) that ∂_t (2.4*a*) = (2.3*a*). Also one finds ∂_t (2.4*b*) = (2.3*b*) through use of $\mathrm{I}_0' = \mathrm{I}_1$, $\mathrm{K}_0' = -\mathrm{K}_1$ and the fact that $\mathrm{I}_0(z)$ satisfies $z^2\mathcal{I}_0'' + z\mathcal{I}_0' - z^2\mathcal{I}_0 = 0$ and $\mathrm{K}_0(z)$ too. Since we have just shown that everywhere $\partial_t G_H = G_\delta$ and G_δ given by (1.3) has the correct limiting behaviour on the east–west axis, our expression for G_H (1.4) reduces there to (2.4*a*) and (2.4*b*). This has been verified independently with a Taylor series expansion of G_H about $\theta = 0$ and $\theta = \pm\pi$.

4. Properties of the Green's functions

In the integral expressions (2.1) and (2.5*a*) for G_δ and (2.2) and (2.5*b*) for G_H, the arguments of the integrands contain the similarity variable βtr. Our new expressions for G_δ (1.3) and for G_H (1.4) also contain this variable via the complex conjugate variables $z_\pm$ defined in (1.5). If time t and distance r were dimensional, the combination βtr is a non-dimensional variable. The mathematical problem has however already been formulated with non-dimensional time t and r or $\{x, y\}$ through scaling with some time scale T and length scale L, i.e. in (1.2*a–c*) the variables are actually non-dimensional $\tilde{t} = t/T$ and $\{\tilde{x}, \tilde{y}\} = \{x/L, y/L\}$ and non-dimensionally $\tilde{\beta} = \beta \times TL$. For convenience we have however dropped the tildes. In the graphs below we shall plot the response against non-dimensional $\{x, y\}$ and time t scaled with arbitrary L and T but in the numerical evaluations we have set $\beta = 1$.

4.1. *Response to impulsive forcing: G_δ*

Graphing the exact solution G_δ given in (1.3) is easy with available numerical packages although some care is required on the western axis where $\theta = \pm\pi$. Due to ambiguity as to how the Bessel functions behave as their arguments become purely imaginary ($z_\pm = \pm \mathrm{i}\sqrt{\beta tr}$), it is best to use a numerical grid that has no points exactly on the western axis. Since spatially the response depends only on the similarity coordinates βtx, βty or βtr and θ, for any $t = t_0 > 0$ all information is contained in the response at t_0. But it is illuminating to graph the response as a function of time. As mentioned in the introduction, very little effort is required to create a movie that vividly illustrates the evolution.

Thus in figure 3 we chose non-dimensional time $t = t_0 = 0.25$ (*a*) and $t = 2t_0 = 0.5$ (*b*). In (*a*) we have drawn a circle with radius $r_0 = 50$ and in (*b*) with radius $r = (1/2)r_0 = 25$. Therefore in both panels the circles have $tr = t_0 r_0$ and the self-similarity is evident: in figure 3(*b*) the same pattern is seen within the circle as in figure 3(*a*) but shrunk to half the scale. For increasing time more of the 'banana' shaped regions appear to propagate from the east towards the source location indicated by '●'. An ever larger number gets wrapped about the origin, with increasing curvature.

West of the source a wake-like region exists forever concentrated about the western axis. In figure 3(*a*) the boundary of the wake is indicated by the dashed curve along which $G_\delta = 0$. Within this region, all streamlines indicate flow with the same sense of circulation about the origin but elongated in the western direction. East of the source, contours near the east–west axis are nearly north–south thus indicating predominantly north–south motions with velocity v advecting planetary vorticity. In the white area in figure 3 near the source location, the response exceeds some arbitrarily chosen

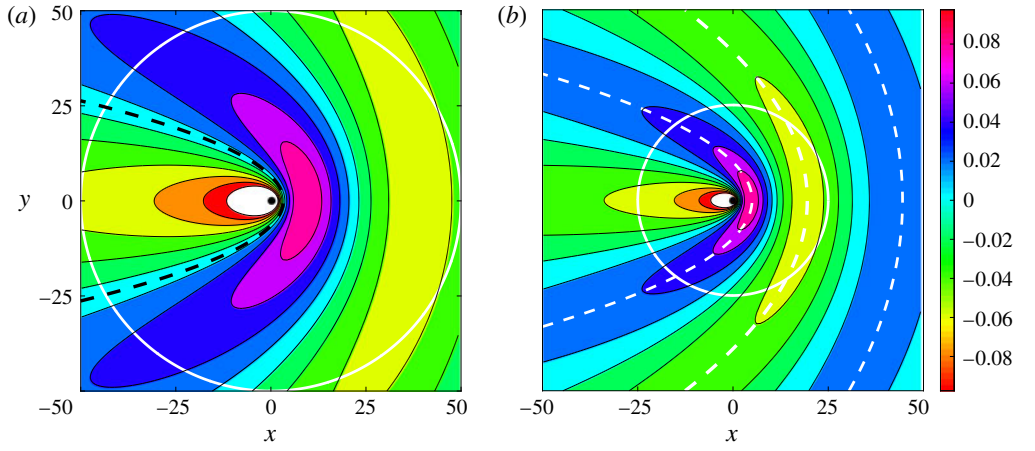

FIGURE 3. Contours of G_δ (1.3) at (*a*) non-dimensional time $t = 0.25$ and (*b*) $t = 0.5$. White circle in (*a*) has a radius $r = 50$ and in (*b*) a radius $r = 25$. Because of self-similarity in (*b*) at the double the time compared to (*a*), the pattern within the circle is exactly the same. Black dot ● at the centre $r = 0$ indicates the source origin. White space thereabouts indicates extreme negative values associated with the logarithmic singularity of G_δ (see text). In (*a*) the black dashed line is the parabola $2a\zeta = \pi/2$ with $\zeta = \sqrt{x + r}$ and $a = \sqrt{\beta t/2}$. Along this contour $G_\delta = 0$. In (*b*) the white dashed parabolas are $2a\zeta = (n + 1)\pi$ with $n = 0, 1, 2$.

(negative) amplitude threshold. Veronis (1958) was already able to sketch these patterns by numerically solving a partial differential equation similar to (2.13*b*) (see also Longuet-Higgins 1965). Near the source location (the white region in figure 3), according to (3.15) the singular behaviour persists.

With the known properties

$$z \to \infty: \quad \mathrm{J}_\nu(z) \sim \sqrt{2/(\pi z)}\cos(z - \tfrac{1}{2}\nu\pi - \tfrac{1}{4}\pi), \quad \mathrm{Y}_\nu(z) \sim \sqrt{2/(\pi z)}\sin(z - \tfrac{1}{2}\nu\pi - \tfrac{1}{4}\pi), \tag{4.1a,b}$$

according to (1.3)

$$\beta t r \to \infty: \quad G_\delta \sim -\frac{\cos(z_+ + z_-)}{2\pi\sqrt{z_+ z_-}}. \tag{4.2}$$

With the definitions of $z_\pm$ in (3.7) and the parabolic coordinates $\{\zeta, \eta\}$ in (3.8):

$$\beta t r \to \infty: \quad G_\delta \sim -\frac{\cos(2a\zeta)}{2\pi\sqrt{a^2(\zeta^2 + \eta^2)}} = -\frac{\cos(\sqrt{2\beta t(x + r)})}{2\pi\sqrt{\beta t r}} \equiv G^a_\delta. \tag{4.3}$$

Lines of constant $\zeta = \sqrt{x + r}$ are parabolas that open towards the west ($x < 0$) as shown in figure 2. Some of these parabolas have been drawn in figure 3 as dashed curves. Longuet-Higgins (1965) already predicted that lines of constant phase would be such parabolas. The approximation G^a_δ in (4.3) was recently found by Webb, Duba & Hu (2016), but as the large-time behaviour implied by an (inverse Laplace transform) integral representation of G_δ.

The approximation (4.3) predicts zeros for $2a\zeta = (n + 1/2)\pi$ ($n = 0, 1, \ldots$). The first zero ($n = 0$) has $2a\zeta = \pi/2$ which has been drawn in figure 3(*a*) as the dashed black parabola, delineating the 'wake'. The approximation predicts on the eastern side

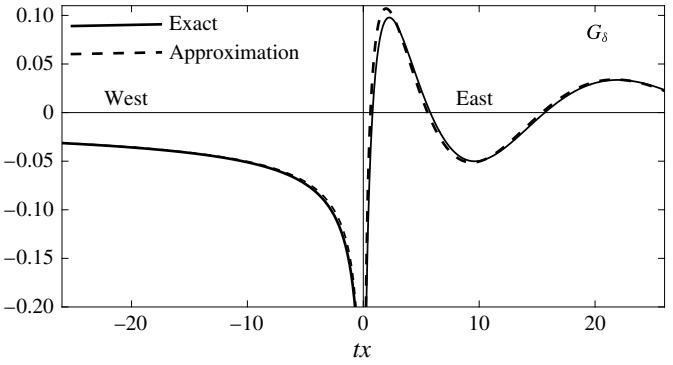

FIGURE 4. Graph showing the exact G_δ (1.3) on the east–west axis through the source and the approximation G^a_δ (4.4*a*,*b*). According to (2.3*a*) to the east: $G_\delta = \mathrm{J}_0(\rho)\mathrm{Y}_0(\rho)/2$ and to the west according to (2.3*b*) $G_\delta = -\mathrm{I}_0(\rho)\mathrm{K}_0(\rho)/\pi$ with $\rho = \sqrt{\beta t|x|}$. For convenience we used $\beta = 1$.

maxima/minima for $2a\zeta = (n+1)\pi$. For $n = 0, 1, 2$ these are the three white dashed parabolas drawn in figure 3(*b*). It is seen that they form the 'spine' of the curved patterns.

The approximation reveals the salient behaviour for large βtr that is hidden in the exact but complex expression (1.3) for G_δ. For large βtr or $\beta t|x|$ on the east–west axis

$$\theta = 0\,(\text{east}):\quad G^a_\delta = -\frac{\cos(2\sqrt{\beta tr})}{2\pi\sqrt{\beta tr}},\qquad \theta = \pm\pi\,(\text{west}):\quad G^a_\delta = -\frac{1}{2\pi\sqrt{\beta tr}}. \quad (4.4a,b)$$

In figure 4 we compare the approximation on this axis with the known exact solution(s) (2.3*a*,*b*). This cross-section along the axis illustrates some of the features seen in figure 3. In particular, the first zero crossing with $2a\zeta = 2\sqrt{\beta tx} = (1/2)\pi$ on the eastern side corresponds to the 'wake' defined by $G_\delta = 0$ (the black parabola in figure 3*a*).

4.2. *Response to sustained forcing: G_H*

In figure 5 we show contours of the exact solution G_H given in (1.4) for non-dimensional times $t = t_0 = 0.5$ (*a*) and $t = 2t_0 = 1$. As in figure 3 for G_δ, we have drawn in (*a*) a circle with radius $r_0 = 50$ and in (*b*) with radius $r = (1/2)r_0 = 25$. In both panels the circles have $tr = t_0 r_0$ and spatial self-similarity is evident. The source location is again indicated by '●'. Close to the source according to (3.21) with increasing time the singularity grows in amplitude, if this can be said in regard to something that has infinite amplitude. Within the white areas in figure 5, G_H exceeds some (negative) amplitude threshold associated with this singularity.

According to (4.1), for large arguments $|z_\pm| \gg 1$, the terms within square brackets in (1.4) become

$$\left.\begin{aligned} z_+[\mathrm{J}_1(z_+)\mathrm{Y}_0(z_-) + \mathrm{J}_0(z_-)\mathrm{Y}_1(z_+)] &\sim -\frac{2}{\pi}\frac{z_+}{\sqrt{z_+z_-}}\sin(z_+ + z_-),\\ z_-[\mathrm{J}_1(z_-)\mathrm{Y}_0(z_+) + \mathrm{J}_0(z_+)\mathrm{Y}_1(z_-)] &\sim -\frac{2}{\pi}\frac{z_-}{\sqrt{z_+z_-}}\sin(z_+ + z_-). \end{aligned}\right\} \quad (4.5)$$

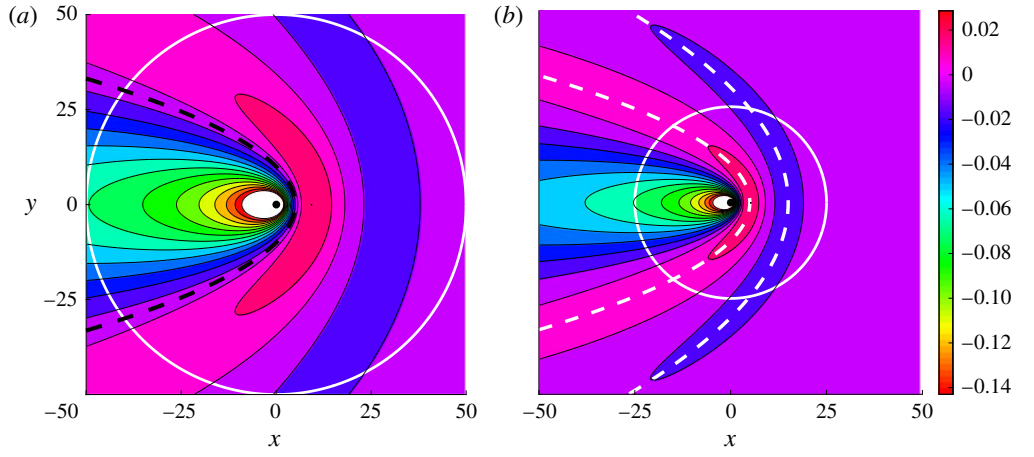

FIGURE 5. Contours of G_H at (a) non-dimensional time $t = 0.5$ and (b) $t = 1.0$. White circle in (a) has a radius $r = 50$ and in (b) a radius $r = 25$. In (a) the black dashed line is the parabola $2a\zeta = \pi$ with $\zeta = \sqrt{x + r}$ and $a = \sqrt{\beta t/2}$. Along this curve $G_H = 0$. In (b) the white dashed lines are for $2a\zeta = (n + 3/2)\pi$ with $n = 0, 1$.

Putting (4.5) in (1.4) yields

$$\beta tr \to \infty: \quad G_H \sim -\frac{1}{\pi} \frac{t \sin(z_+ + z_-)}{(z_+ + z_-)\sqrt{z_+ z_-}} \tag{4.6}$$

and with (3.7), equation (3.8)

$$\beta tr \to \infty: \quad G_H \sim -\frac{1}{\pi} \frac{\sin(2a\zeta)}{\beta\zeta\sqrt{\zeta^2 + \eta^2}} = -\frac{\sin(\sqrt{2\beta t(x + r)})}{\pi\beta\sqrt{x + r}\sqrt{2r}} \equiv G_H^a. \tag{4.7}$$

This agrees with the result of Kamenkovich (1989) who derived large time expansions of G_H via a consideration of the asymptotic properties of inverse Laplace transforms. There is a noticeable difference between G_δ and G_H: whereas according to (4.3) amplitudes of G_δ decay with time as $t^{-1/2}$, amplitudes of G_H are constant (with the exception of the west axis; see below). Nonetheless $G_\delta = \partial G_H/\partial t$ and one easily verifies with (4.3) and (4.7) that also $G_\delta^a = \partial G_H^a/\partial t$.

The approximation (4.7) predicts zeros for $2a\zeta = (n + 1)\pi$ ($n = 0, 1, \ldots$) and again $\zeta = \sqrt{x + r}$ and $a = \sqrt{\beta t/2}$. The first zero has $2a\zeta = \pi$ and the 'wake' defined by this curve on which $G_H = 0$ is the black dashed line in figure 5(a). The approximation predicts on the eastern side maxima/minima for $2a\zeta = (n + 3/2)\pi$. The first two ($n = 0, 1$) are the dashed parabolas drawn in figure 5(b).

Comparison of figure 5 with figure 3 reveals a difference: in figure 5 the response to the east of the forcing appears to contain fewer of the typical patterns. Why this is can be illustrated with the far field approximation of G_H given by (4.7), i.e. for large βtr on the east–west axis:

$$\theta = 0 \text{ (east)}: \quad G_H^a = -\frac{\sin(2\sqrt{\beta tr})}{2\pi\beta r}, \quad \theta = \pm\pi \text{ (west)}: \quad G_H^a = -\frac{1}{\pi}\sqrt{\frac{t}{\beta r}}. \tag{4.8a,b}$$

In figure 6 we compare the approximation on the entire axis with the exact solution(s) (2.4a,b). This explains why in figure 5 there are fewer of the parabolically

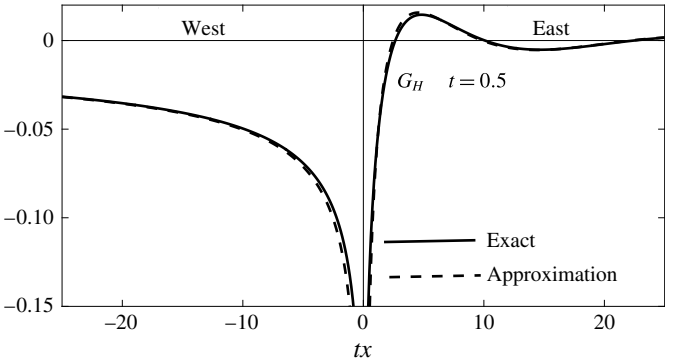

FIGURE 6. Graph showing the exact G_H (1.4) on the east–west axis through the source and the approximation G_H^a (4.8*a*,*b*) at non-dimensional time $t = 0.5$. According to (2.4*a*) to the east: $G_H = t[\mathrm{J}_0(\rho)\mathrm{Y}_0(\rho) + \mathrm{J}_1(\rho)\mathrm{Y}_1(\rho)]/2$ and to the west according to (2.4*b*) $G_H = -t[\mathrm{I}_0(\rho)\mathrm{K}_0(\rho) + \mathrm{I}_1(\rho)\mathrm{K}_1(\rho)]/\pi$ with argument $\rho = \sqrt{\beta t|x|}$.

shaped regions visible east of the forcing: on the eastern axis for fixed time (4.4*a*) reveals that $G_\delta \propto 1/\sqrt{r}$ whereas (4.8*a*) indicates $G_H \propto 1/r$, i.e. G_H decays more rapidly towards the east than G_δ with distance r from the source location. The two prominent patterns east of the source seen in figure 5(*a*) correspond to the first maximum and minimum in the cross-section shown in figure 6, i.e. $2a\zeta = 2\sqrt{\beta t x} = (n + 3/2)\pi$ and $n = 0, 1$. Finally, note that (4.6) shows that amplitudes do not decay or grow with time t except exactly on the west axis ($\zeta = 0$) where

$$\zeta \downarrow 0: \quad \frac{\sin(2a\zeta)}{\zeta} \to 2a = \sqrt{2\beta t} \tag{4.9}$$

and this singular limit leads to the unbounded growth of G_H displayed in (4.8*b*).

4.3. *Kinetic energy distributions*

The approximation (4.3) suggests that at a fixed location with increasing time, the quasi-wave field associated with G_δ disappears with $1/\sqrt{t}$. Thus, nothing but the singularity (3.15) would remain. But a more relevant quantity is kinetic energy E. This is determined by gradients of the streamfunction $\psi = G_\delta$ and because with increasing time the spatial scales decrease, gradients increase. This compensates for the overall decrease of the amplitude of G_δ.

The kinetic energy associated with the Green's function is $E = (1/2)\nabla G \cdot \nabla G$. The easiest way to calculate E is to use the fact that in parabolic coordinates

$$\nabla = \frac{1}{\sqrt{\zeta^2 + \eta^2}}\left[\hat{\zeta}\frac{\partial}{\partial\zeta} + \hat{\eta}\frac{\partial}{\partial\eta}\right], \tag{4.10}$$

with $\{\hat{\zeta}, \hat{\eta}\}$ the orthogonal unit vectors associated with $\{\zeta, \eta\}$ (see Morse & Feshbach 1953; Moon & Spencer 1961). Without going into any further details, we find

$$\begin{aligned} E &= \frac{1}{2(\zeta^2 + \eta^2)}\left[\left(\frac{\partial G}{\partial\zeta}\right)^2 + \left(\frac{\partial G}{\partial\eta}\right)^2\right] \\ &= \left(\frac{1}{4}\right)^2 \frac{\beta t}{\zeta^2 + \eta^2}|\mathrm{J}_0(z_+)\mathrm{Y}_1(z_-) + \mathrm{J}_1(z_-)\mathrm{Y}_0(z_+)|^2 = E_\delta \end{aligned} \tag{4.11}$$

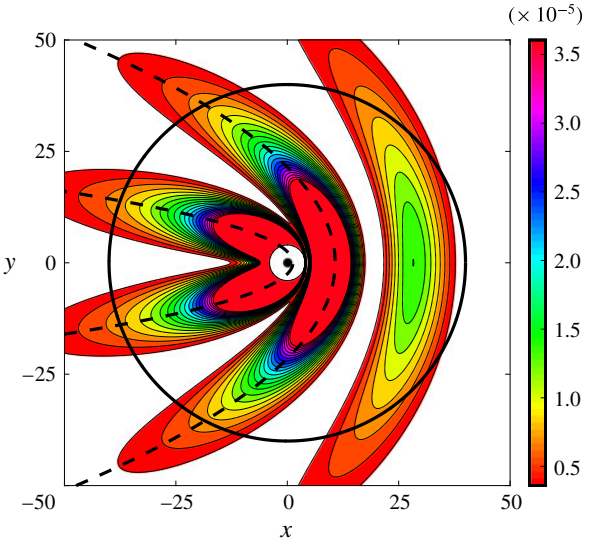

FIGURE 7. Contours of kinetic energy E_δ given by (4.11) at $t=0.5$. The innermost dashed parabola is defined by $2a\zeta = (n+1/2)\pi$ with $n=0$ and $\zeta = \sqrt{x+r}$, $a=\sqrt{\beta t/2}$. This corresponds to the 'wake' boundary shown in figure 3(*a*) along which $G_\delta = 0$. The second parabola is for $n=1$. Energy along the circle with radius $r=40$ is shown in figure 8.

when $G = G_\delta$ given by (1.3) is substituted in (4.11). This may give the impression that the kinetic energy grows with time t. But, for large βtr it follows with (4.1) that

$$\beta tr \to \infty: \quad \mathrm{J}_0(z_+)\mathrm{Y}_1(z_-) + \mathrm{J}_1(z_-)\mathrm{Y}_0(z_+) \sim -\frac{2}{\pi}\frac{\sin(z_+ + z_-)}{\sqrt{z_+ z_-}}. \tag{4.12}$$

Squaring (4.12) and substitution in (4.11) yields for large βtr the approximation

$$E_\delta \sim \frac{1}{2}\frac{\sin^2(2a\zeta)}{\pi^2(\zeta^2+\eta^2)^2} = \frac{1}{2}\frac{\sin^2(\sqrt{2\beta t(x+r)})}{(2\pi r)^2} \equiv E_\delta^a. \tag{4.13}$$

In figure 7 we show contours of kinetic energy E_δ (4.11). The patterns are similar to that of G_δ shown in figure 3. The one-term approximation (4.13) predicts maximal energy along parabolas $2a\zeta = (n+1/2)\pi$ with $n=0, 1, \ldots$ ($\zeta = \sqrt{x+r}$, $a=\sqrt{\beta t/2}$). In figure 7 the innermost dashed parabola is for $n=0$ and coincides with the wake boundary shown in figure 3(*a*). This is a location of maximal kinetic energy. In figure 7 the second parabola ($n=1$) is seen to match the next pattern of maximal energy well. In figure 7 we have drawn a circle with radius $r=40$. Going around this circle of radius $r=40$ the peaks of energy are shown in figure 8 as well as for a circle of smaller radius $r=30$. The approximation (4.13), based on the assumption $\beta tr \gg 1$, shows that at large r all maxima will have the same amplitude, as observed in figure 8. In polar coordinates the approximation

$$E_\delta^a = \frac{1}{2}\frac{\sin^2(2a\zeta)}{(2\pi r)^2}, \quad 2a\zeta = \sqrt{2\beta tr}\sqrt{1+\cos\theta} \tag{4.14}$$

shows that the energy peaks decay with distance $1/r^2$ from the source and the peak positions in terms of the polar angle θ are determined by $2\beta tr(1+\cos\theta) = (n+1/2)^2\pi^2$. At fixed radius r with increasing time t more peaks appear as continuously

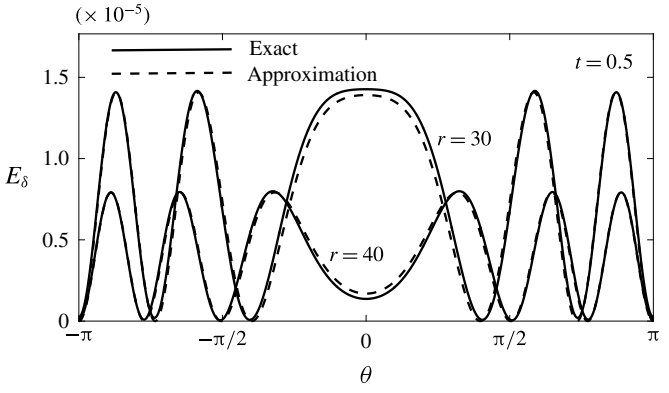

FIGURE 8. Kinetic energy E_δ (4.11) and the approximation E_δ^a (4.13) along circles of radius $r=30$ and $r=40$ at $t=0.5$. The circle $r=40$ is shown in figure 7.

more of the parabolic patterns seen in figure 3 coming from the eastern side get wrapped about the forcing origin.

The energy associated with G_H can be calculated exactly too and we find

$$\frac{\partial G_H}{\partial \eta} = \frac{1}{\eta}\left\{t(G_\delta + \tfrac{1}{4}[\mathrm{J}_1(z_+)\mathrm{Y}_1(z_-) + \text{c.c.}]) - G_H\right\}, \tag{4.15a}$$

$$\frac{\partial G_H}{\partial \zeta} = \frac{1}{\zeta}\{t(G_\delta - \tfrac{1}{4}[\mathrm{J}_1(z_+)\mathrm{Y}_1(z_-) + \text{c.c.}]) - G_H\}, \tag{4.15b}$$

with G_δ as in (1.3) and G_H again given by (1.4). Division by η in (4.15*a*) may be cause of concern at first sight, but $\eta=0$ corresponds to the east axis and there according to (2.3*a*) and (2.4*a*):

$$\left.\begin{array}{rl} \eta=0 \text{ (east):} & G_\delta = \tfrac{1}{2}\mathrm{J}_0(\rho)\mathrm{Y}_0(\rho), \quad G_H = \tfrac{1}{2}t[\mathrm{J}_0(\rho)\mathrm{Y}_0(\rho) + \mathrm{J}_1(\rho)\mathrm{Y}_1(\rho)], \\ \text{and} & \tfrac{1}{4}[\mathrm{J}_1(z_+)\mathrm{Y}_1(z_-) + \text{c.c.}] = \tfrac{1}{2}\mathrm{J}_1(\rho)\mathrm{Y}_1(\rho), \quad \rho = \sqrt{\beta t r} \end{array}\right\} \tag{4.16}$$

so that in the limit $\eta=0$ the numerator of (4.15*a*) vanishes and an expansion in small η can be shown to give a finite answer for $\partial G_H/\partial\eta$. Also the limit $\zeta=0$ appears dangerous in (4.15*b*) but again a finite answer is obtained by taking into account that there

$$\left.\begin{array}{rl} \zeta=0 \text{ (west):} & G_\delta = -\dfrac{\mathrm{I}_0(\rho)\mathrm{K}_0(\rho)}{\pi}, \quad G_H = -\dfrac{t}{\pi}\left[\mathrm{I}_0(\rho)\mathrm{K}_0(\rho) + \mathrm{I}_1(\rho)\mathrm{K}_1(\rho)\right], \\ & \tfrac{1}{4}[\mathrm{J}_1(z_+)\mathrm{Y}_1(z_-) + \text{c.c.}] = \dfrac{\mathrm{I}_1(\rho)\mathrm{K}_1(\rho)}{\pi}, \quad \rho = \sqrt{\beta t r}. \end{array}\right\} \tag{4.17}$$

Therefore in the limit $\zeta=0$ the numerator of (4.15*b*) vanishes and $\partial G_H/\partial\zeta$ is well defined. Contours of

$$E_H = \frac{1}{2(\zeta^2+\eta^2)}\left[\left(\frac{\partial G_H}{\partial \zeta}\right)^2 + \left(\frac{\partial G_H}{\partial \eta}\right)^2\right] \tag{4.18}$$

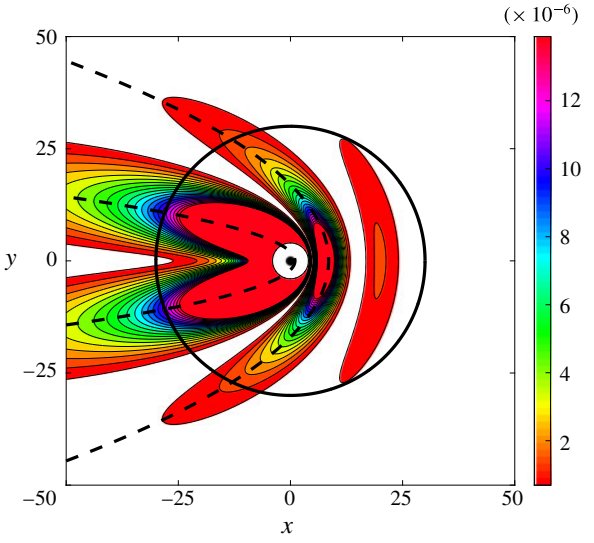

FIGURE 9. Contours of energy E_H according to (4.18) at $t = 1$. The innermost dashed parabola is for $2a\zeta = \sqrt{2}$ with $\zeta = \sqrt{x + r}$, $a = \sqrt{\beta t/2}$. This lies inside to the 'wake' boundary shown in figure 5(*a*) along which $G_H = 0$ and for which $2a\zeta = \pi$. Energy along the circle with radius $r = 30$ is shown in figure 10.

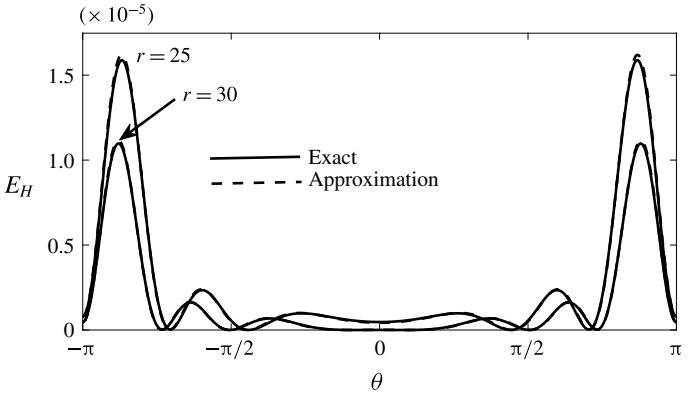

FIGURE 10. Contours of kinetic energy E_H (4.18) at $t = 1$ and the approximation E_H^a (4.19) along circles of radius $r = 25$ and $r = 30$ at $t = 1$. The circle $r = 30$ is shown in figure 9.

are shown in figure 9. The energy along the circle with radius $r = 30$ drawn in figure 9 is shown in figure 10.

Whereas it is easy to find the approximation (4.13) for the kinetic energy E_δ by employing the asymptotic properties of $\mathrm{J}_\nu, \mathrm{Y}_\nu$ according to (4.1), things become quite difficult if the same route is taken here for E_H: it requires the rarely used higher-order corrections to (4.1). Instead we calculate the approximation by differentiation of (4.7).

This yields in polar coordinates

$$E_H \sim \frac{1}{2}\frac{1}{(2\pi r)^2}\left(\frac{t}{\beta r}\right)\frac{1}{1+\cos\theta}\left[2\cos^2(2a\zeta) - \frac{2(3+\cos\theta)\cos(2a\zeta)\sin(2a\zeta)}{(2a\zeta)} + \frac{(5+3\cos\theta)\sin^2(2a\zeta)}{(2a\zeta)^2}\right] \equiv E_H^a, \quad 2a\zeta = \sqrt{2\beta t}\sqrt{r(1+\cos\theta)}. \tag{4.19}$$

For large time the first term within square brackets, $\cos^2(2a\zeta)$, dominates but the next two terms cannot be discarded: they are both required to negate the singular behaviour of the prefactor $1/r(1+\cos\theta) = 1/\zeta^2$. In other words, in the limit $\theta = \pm\pi$ or $\zeta = 0$ (the western axis) all three terms are required. In that limit $\sin(2a\zeta)/(2a\zeta) \to 1$ and the bracketed term in (4.19) evaluates to

$$[2 - 2(3-1) + (5-3)] = 0 \tag{4.20}$$

and expansions of the second and third term in powers of small ζ always yield a finite result. In figure 10 we compare the approximation (4.19) with the exact energy along the circle of radius $r = 30$ also shown in figure 9 and at a smaller radius $r = 25$. We simply chose $t = 1$ which was also used for figure 5(*b*). Comparison of figures 9 and 10 with the corresponding figures 7 and 8 for G_δ reveals that for G_H the kinetic energy is dominated by two plumes on the western side of the forcing. Another differences is that (4.19) shows that away from the western axis, E_H decays with distance from the forcing with $1/r^3$ while linearly growing in time while (4.13) shows that E_δ decays with $1/r^2$ with amplitudes that are independent of time.

Finally, as in figure 7 for E_δ we have drawn in figure 9 two parabolas $\zeta = \text{const.}$ that fit the maximal energy patterns. For G_δ in figure 7 the innermost parabola coincided with the wake boundary $G_\delta = 0$ and $2a\zeta = (1/2)\pi$: this is the first maximum of the leading-order term $\sin^2(2a\zeta)$ in (4.14). But for E_H the first maximum is not determined by $\cos^2(2a\zeta)$ with maxima at $2a\zeta = (n+1)\pi$ but by the combination of all three terms within the square brackets in (4.19). We find that the parabolic axis through the dominant energy pattern in figure 9 lies well within the wake region: in figure 5(*a*) the wake boundary (dashed parabola) is defined by $2a\zeta = \pi$ but in figure 9 the axis was found to coincide with $2a\zeta = \sqrt{2} < \pi$ and the second parabola with $2a\zeta = 4 < 2\pi$. At later times (not shown) the tendency is that the axis of the dominant energy 'plumes' of E_H moves further towards the west axis, i.e. further into the interior of the wake region.

5. Discussion

In this paper we have shown that two-dimensional Green's functions G_δ and G_H given by (1.3) and (1.4), respectively, solve the forced Rossby wave equation (1.2). Previously only known via integral representations, these new compact expressions provide a complete description of the response. They reduce on the east–west axis to the long-known exact expressions discussed in § 2, i.e. (2.3*a*,*b*) for G_δ and (2.4*a*,*b*) for G_H and far from the forcing location to the asymptotic forms (4.3) and (4.7), respectively. The latter were also known via transform methods but here they arise directly from the properties of the Bessel functions $\mathrm{J}_n(z)$, $\mathrm{Y}_n(z)$ for large (complex) arguments z.

Exact explicit expressions for Green's functions were known in one-dimensional (Cahn 1945; Rossby 1945) and three-dimensional (Dickinson 1969*a*,*b*) settings only.

Usually solutions of the forced problem are sought through transform methods (see Veronis 1958; Longuet-Higgins 1965; Kamenkovich 1989; Llewellyn-Smith 1997 but also the recent studies by McKenzie 2014; Webb *et al.* 2016). In two-dimensional problems this has led to integral representations like those mentioned in § 2.

A crucial development has been that the integral representation for G_δ can be written as (3.1). From this the closed-form expression (1.3) for G_δ followed via the work of Dixon & Ferrar (1933) as discussed in § 3. The validity of this solution has been verified in § 3.1 and in § 3.2 we derived and verified the expression (1.4) for G_H. This becomes very efficient through the introduction of the complex conjugate variables $z_\star = \zeta + \mathrm{i}\eta$, $\bar{z}_\star = \zeta - \mathrm{i}\eta$ defined in (3.7). In particular, the Rossby wave operator then assumes the symmetric form given in (3.11). That contour patterns of G_δ and G_H shown in § 4 in figures 3 and 5 coincide largely with the parabolas $\zeta = \sqrt{r + x} = \text{const.}$ is perhaps not surprising since if on the right-hand side of (1.2*a*) instead of $\delta(t)$ periodic forcing $\exp(\mathrm{i}\omega t)$ is assumed, lines of constant phase are also $\zeta = \text{const.}$ (see Rhines 2003).

The parabolic coordinates $\{\zeta, \eta\}$ are of wider interest in the context of non-divergent Rossby waves. First note that the form of $\mathcal{L}$ in (3.10) suggests that there is no real distinction between ζ and η whereas in the Cartesian $\{x, y\}$ formulation longitude x introduces an 'asymmetry' not obvious in (3.10) except for the sign difference between the ζ and η terms multiplying β (the same spatial part of this Rossby wave operator for a steady, frictional version of the vorticity equation was previously considered in ocean circulation context in Maas (1989), Zimmerman & Maas (1989) and Boyd & Sanjaya (2014)). Let us further note that in as much that the Green's functions are streamfunctions ψ with the associated velocity components $u = -\partial_y\psi$, $v = \partial_x\psi$, equation (2.13*b*) is simply

$$\partial_t(xu + yv) + \frac{1}{2}\beta y\,\psi = 0, \quad \text{with } xu + vy = \boldsymbol{u}\cdot\boldsymbol{r}, \quad \boldsymbol{u} = u\boldsymbol{i} + v\boldsymbol{j},\ \boldsymbol{r} = x\boldsymbol{i} + y\boldsymbol{j} \tag{5.1}$$

and $\{\boldsymbol{i}, \boldsymbol{j}\}$ the customary unit vectors associated with $\{x, y\}$. The projection of the velocity vector $\boldsymbol{u}$ on the position vector $\boldsymbol{r}$ is $\boldsymbol{u}\cdot\boldsymbol{r} = ru_r$ with u_r the radial velocity component in cylindrical coordinates (see figure 1). In other words, in the wave field associated with the Green's functions the radial velocity component evolves according to $\partial_t ru_r + (1/2)\beta y\psi = 0$. It is not clear to us whether this has a physical meaning. However, leaving out a common factor 1/2, in parabolic coordinates (5.1) becomes

$$\frac{\partial}{\partial t}\left(\eta\frac{\partial}{\partial\zeta} - \zeta\frac{\partial}{\partial\eta}\right)\psi + \beta\zeta\eta\psi = 0. \tag{5.2}$$

Further, differentiation of (5.1) with respect to x and multiplication of the Rossby wave equation by y allows for the elimination of the β-terms which results in

$$\partial_t\{y\nabla^2 + 2\partial_x(x\partial_y - y\partial_x)\}\psi = 0 \tag{5.3}$$

but in the parabolic coordinates (5.3) assumes the form

$$\frac{\partial}{\partial t}\left\{\frac{\partial^2}{\partial\zeta\,\partial\eta} + \frac{\eta}{\zeta^2+\eta^2}\frac{\partial}{\partial\zeta} + \frac{\zeta}{\zeta^2+\eta^2}\frac{\partial}{\partial\eta}\right\}\psi = 0. \tag{5.4}$$

Remarkably, integrating (5.4) in time shows that the Green's functions are determined by a second-order partial differential equation, which, moreover, is entirely symmetric

in parabolic coordinates ζ, η. Additionally, the form of the Rossby wave operator $\mathcal{L}$ (3.10) in these coordinates suggests that the parabolic coordinates are rather 'natural' coordinates for non-divergent Rossby waves.

This raises the question why the response in the forced problem considered here is dominated by the westward parabolas $\zeta = \sqrt{r+x}$ while the opposite parabola $\eta = \sqrt{r-x}$ only plays a role in providing overall amplitude attenuation via inverse (fractional) powers of $r = (1/2)(\zeta^2 + \eta^2)$. This can be understood with the analyses of Longuet-Higgins (1965) and the more recent work by McKenzie (2014), i.e. via considerations of the dispersion relation for monochromatic waves, the group velocity and the method of stationary phase. But a cursory examination of the properties of $\mathcal{L}$ in parabolic coordinates, i.e. (3.10), indicates that free, parabolically shaped Rossby waves following lines of constant $\eta = \sqrt{r-x}$ instead of $\zeta = \sqrt{r+x}$ do also exist at any given frequency. The repercussions of this observation are left for a future study.

A few final remarks are in order: the singular behaviour found for G_δ in (3.15) and G_H in (3.21) at the forcing location persists. For G_H this is not surprising since the forcing is maintained but for G_δ this is counterintuitive since one can interpret G_δ for some $t = t_0 > 0$ as a given initial streamfunction $\psi_0(x, y) = \psi(x, y, t_0)$. This initial condition for $t = t_0$ can be developed in plane Rossby waves with the spectrum $A_0(k, l)$ and for $t > t_0$ the field would evolve as

$$\psi(x, y, t) = \iint A_0(k, l) \mathrm{e}^{\mathrm{i}(\omega t - kx - ly)} \, \mathrm{d}k \, \mathrm{d}l, \tag{5.5}$$

with ω satisfying the well-known dispersion relation

$$\omega = -\frac{\beta k}{k^2 + l^2}. \tag{5.6}$$

Without explicitly knowing the spectrum $A_0(k, l)$, one would think that dispersion leads to the disappearance of the singularity. But it does not. The 'shrinking' of the patterns via the similarity variable $\beta t r$ towards the origin is also baffling although one might see this as a confirmation of the long-known properties of the Rossby waves: short waves (small spatial scales) have small group velocities (Pedlosky 1987).

The Rossby wave equation describes the time evolution of vorticity q which for the Green's functions is $q = \nabla^2 G$. This can be calculated quickly. For example, with the variables $\{z_\star, \bar{z}_\star\}$, introduced in (3.7),

$$\nabla^2 = \frac{4}{z_\star \bar{z}_\star} \frac{\partial^2}{\partial z_\star \partial \bar{z}_\star} \quad \text{and} \quad q_\delta \equiv \nabla^2 G_\delta = \frac{\beta t}{4r} [\mathrm{J}_1(z_+)\mathrm{Y}_1(z_-) + \mathrm{J}_1(z_-)\mathrm{Y}_1(z_+)] \tag{5.7a,b}$$

after substitution of (1.3) and using $\mathrm{J}_0' = -\mathrm{J}_1$, $\mathrm{Y}_0' = -\mathrm{Y}_1$. For large arguments, i.e. far from the forcing, apart from a constant prefactor, q_δ behaves as $\cos(2a\zeta)/r^{3/2}$. The asymptotic energy distribution given in (4.14) behaves as $\sin^2(2a\zeta)/r^2$ and we thought that perhaps the 'empty' spaces seen in the energy distribution in figure 7 might be filled by $r \times \mathcal{E}_\delta$ with enstrophy $\mathcal{E}_\delta = (1/2)q_\delta^2$ so that a conservation law of the form $\partial_t(E_\delta + r\mathcal{E}_\delta) = 0$ would follow. This was nearly so, but not exactly. Thus we have no good understanding yet of the E_δ pattern seen in figure 7 nor of the energy distribution E_H in figure 9. A proper energy flux formulation is lacking in terms of recognizable physical quantities (see also Rhines 1975). At best we can draw attention to the salient differences between E_δ and E_H: whereas figures 7 and 8 show that at any distance and given time t peaks of energy E_δ have equal amplitude and occur both west and east

of the forcing, figures 9 and 10 show that the energy E_H associated with the sustained forcing is predominantly found west of the forcing. The peak amplitudes of E_δ do not vary with time t while with distance r from the source $E_\delta \propto 1/r^2$ (see (4.14)) but E_H grows with time t and decays more rapidly, i.e. $E_H \propto 1/r^3$ (see (4.19)). The temporal behaviour is not surprising in that continued forcing leads to growth in energy but the spatially more confined nature of E_H as compared to that of E_δ is surprising.

In as much in that the barotropic, non-divergent Rossby wave is a small but fundamental element in the realm of theoretical geophysical fluid dynamics, this study may stimulate interest beyond the current study to search for simple closed-form solutions of forced divergent Rossby waves (waves with finite Rossby deformation radius). This introduces finite group velocity for very long waves and more can then perhaps be said about the evolution of energy distributions and may help recognize 'where' wave energy goes. In view of our results there is reason to be optimistic that the complicated integral representation of Veronis (1958) for divergent Rossby waves and the elegant result of Webb *et al.* (2016) can be reduced to simpler expressions.

Another possible strategy is to consider a 'switch-on/switch-off' source, that is, the response G_δ which Veronis (1958) called a 'tweak', followed by an 'anti-tweak'. This will eliminate the singularity at the forcing location and energy will subsequently be finite everywhere. The simplicity of our expression for G_δ (1.3) allows for quick visualization of such a scenario and further mathematical analysis but this too is left for future research.

Acknowledgements

R.C.K. acknowledges support from National Science Foundation grants OCE 10-32256 and OCE 15-38559. We thank two anonymous referees and S. Llewellyn Smith for their insightful comments of the manuscript.

REFERENCES

BOYD, J. P. & SANJAYA, E. 2014 Geometrical effects of western intensification of wind-driven ocean currents: the stommel model, coastal orientation, and curvature. *Dyn. Atmos. Oceans* **65**, 17–38.

CAHN, A. J. 1945 An investigation of the free oscillations of a simple current system. *J. Meteorol.* **2** (2), 113–119.

DICKINSON, R. E. 1969*a* Propagators of atmospheric motions 1. Excitation by point impulses. *Rev. Geophys.* **7** (3), 483–514.

DICKINSON, R. E. 1969*b* Propagators of atmospheric motions 2. Excitation by switch-on sources. *Rev. Geophys.* **7** (3), 515–538.

DIXON, A. L. & FERRAR, W. L. 1933 Integrals for the products of two bessel functions. *Q. J. Math.* **4**, 193–208.

ERDÉLYI, A. (Ed.) 1953 *Higher Transcendental Functions, 3*, vol. 2. McGraw-Hill.

HOUGH, S. S. 1898 On the application of harmonic analysis to the dynamical theory of the tides. Part ii. On the general integration of laplaces dynamical equations. *Phil. Trans. R. Soc. Lond.* A **191**, 139–185.

KAMENKOVICH, V. M. 1989 Development of Rossby waves generated by localized effects. *Oceanology* **29** (1), 1–11.

LLEWELLYN-SMITH, S. G. 1997 The motion of a non-isolated vortex on the beta-plane. *J. Fluid Mech.* **346**, 149–179.

LONGUET-HIGGINS, M. S. 1965 The response of a stratified ocean to stationary or moving wind-systems. *Deep-Sea Res.* **12**, 923–973.

MAAS, L. R. M. 1989 A closed form green function describing diffusion in a strained flow field. *SIAM J. Appl. Maths* **49** (5), 1359–1373.

MAGNUS, W., OBERHETTINGER, F. & SONI, R. P. 1966 *Formulas and Theorems for the Special Functions of Mathematical Physics*, 3rd edn. Springer.

MARGULES, M. 1893 Luftbewegungen in einer rotierenden sphäroidschale (ii. teil). *Sitz. der Math. - Naturwiss. Klasse, Kais. Akad. Wiss., Wien* **102**, 11–56.

MCKENZIE, J. F. 2014 The group velocity and radiation pattern of Rossby waves. *Geophys. Astrophys. Fluid Dyn.* **108** (3), 258–268.

MOON, P. & SPENCER, D. E. 1961 *Field Theory Handbook*. Springer.

MORSE, P. M. & FESHBACH, H. 1953 *Methods of Theoretical Physics*. McGraw-Hill.

OLVER, F. W. J., LOZIER, D. W., BOISVERT, R. F. & CLARK, C. W. (Eds) 2010 *NIST Handbook of Mathematical Functions*. Cambridge University Press.

PEDLOSKY, J. 1987 *Geophysical Fluid Dynamics*, 2nd edn. Springer.

RHINES, P. B. 1975 Waves and turbulence on a beta-plane. *J. Fluid Mech.* **69**, 417–443.

RHINES, P. B. 2003 Rossby waves. In *Encyclopedia of Atmospheric Sciences* (ed. J. R. Holton, J. A. Curry & J. A. Pyle), pp. 1–37. Academic.

ROSSBY, C.-G. 1945 On the propagation of frequencies and energy in certain types of oceanic and atmospheric waves. *J. Meteorol.* **2** (4), 187–204.

ROSSBY, C.-G. & COLLABORATORS 1939 Relations between variations in the intensity of the zonal circulation of the atmosphere and the displacements of the semi-permanent centres of action. *J. Mar. Res.* **2**, 38–54.

VERONIS, G. 1958 On the transient response of a beta-plane ocean. *J. Oceanogr. Soc. Japan* **14** (1), 1–5.

WEBB, G. M., DUBA, C. T. & HU, Q. 2016 Rossby wave green's functions in an azimuthal wind. *Geophys. Astrophys. Fluid Dyn.* **110** (3), 224–258.

ZIMMERMAN, J. T. F. & MAAS, L. R. M. 1989 Renormalized greens function for nonlinear circulation on the β plane. *Phys. Rev.* A **39** (7), 3575–3590.